Scientific paper

Terahertz (THz) Wave Imaging in Civil Engineering to Assess Self-Healing of Fiber-Reinforced Cementitious Composites (FRCC)

Tomoya Nishiwaki[1*], Koshi Shimizu[2], Tadao Tanabe[3], Diane Gardner[4] and Riccardo Maddalena[5]

Received 30 December 2021, accepted 9 January 2023 doi:10.3151/jact.21.58

Abstract

Although numerous studies have proven the effectiveness of self-healing technologies in concrete, its practical application is limited to only few trials. One of the reasons lies in the lack of self-healing in-situ non-destructive evaluation methods as opposed to invasive and extensive laboratory testing. In this study, a novel Terahertz (THz) wave imaging technique is proposed as a simple, non-destructive, and non-contact measurement methodology to quantitatively evaluate the self-healing effectiveness of cementitious materials. Experiments were conducted in fiber-reinforced cementitious composites (FRCC), which confirmed self-healing performance based on a combination of stimulated autogenous and autonomous healing by using supplementary cementitious materials (FRCC), and PVA fibers; the self-healing index was also calculated by using novel THz wave measurement and compared with existing evaluation methods. Simultaneously, sorptivity test and microstructural characterization on damaged and healed specimens were conducted as the conventional methods. As a result, the proposed THz imaging successfully quantified the self-healing performance on cementitious samples. Also, a correlation between the recovery rate (cracked/healed) measured by sorptivity test and THz wave imaging was defined.

1. Introduction

Concrete is the second most used industrial material in the world after water. The majority of our infrastructures, buildings and houses are made of reinforced concrete structures with a design lifespan of up to 100 years. On the other hand, the production process of Portland cement, which is the main raw materials for concrete, is one of the major contributors of CO_2 emissions in the world (Ellis *et al.* 2019). CO_2 emissions from cement production account for approximately 8% of global emissions (Andrew 2019), and reduction of these emissions is strongly sought. One solution to reduce this emission is to replace cement with alternative materials, such as industrial by-products (Schneider *et al.* 2011). Another promising approach is to improve durability and extend the service life of reinforced concrete structures so that the need for demolition and re-build can be halted (Müller *et al.* 2014).

The use of supplementary cementitious materials (SCMs) is one of the most promising and popular methods to replace Portland cement and reduce the unit cement content and subsequent CO_2 emissions (Yang *et al.* 2015). SCMs derive from industrial process, hence their associated CO_2 emissions are very low or negligible. According to the literature, the CO_2 emission from the production of ground granulated blast-furnace slag (GGBS) is 24.1 kg/t, and from the production of fly ash is 17.9 kg/t (JSCE 2002). They are extremely smaller than the CO_2 emission from the Portland cement production, which is 757.9 kg/t, and mainly due to their handling and transportation.

Extending the service life of concrete structures means reducing the need for maintenance whilst ensuring the service requirements are met throughout their life-span. Cracks in reinforced concrete structures not only reduce the structural stiffness, but also provide a pathway for deleterious species to penetrate and diffuse into the concrete. Thus, periodical inspections and continuous maintenance works are needed to maintain the mechanical properties and ensure the structural safety. However, this is not always achievable due to economical costs, location of the structure, shape and other site restrictions. It becomes difficult to conduct comprehensive inspection and maintenance/repair works. Therefore, it is necessary to minimize the occurrence of cracks, and ensure their widths within acceptable values.

Research on self-healing concrete as a way to minimize and/or prevent cracks has attracted attention in recent years (Mihashi and Nishiwaki 2012; De Belie *et al.* 2018). One of the approaches studied is relying on the natural healing phenomenon when concrete is exposed to

[1]Associate Professor, Graduate School of Engineering, Tohoku University, Aoba 6-6-11-1209, Aramaki, Aoba, Sendai, Miyagi 980-8579, Japan. *Corresponding author, *E-mail*: tomoya.nishiwaki.e8@tohoku.ac.jp
[2]Graduate Student, Graduate School of Engineering, Tohoku University, Aoba 6-6-11-1209, Aramaki, Aoba, Sendai, Miyagi 980-8579, Japan.
[3]Professor, College of Engineering and Design, Shibaura Institute of Technology, 3-9-14 Shibaura, Minato-ku, Tokyo 108-8548, Japan.
[4]Reader, School of Engineering, Cardiff University, Cardiff CF24 3AA, UK.
[5]Lecturer, School of Engineering, Cardiff University, Cardiff CF24 3AA, UK.

water, autogenous healing. Crack widths up to 0.1 mm can self-heal in an environment where moisture is supplied (Edvardsen 1999). This is caused by the reaction of carbonate ions (CO_3^{2-}) dissolved in water with calcium ions (Ca^{2+}) in the concrete, precipitating calcite ($CaCO_3$) crystals and hydration of unhydrated particles (Huang *et al.* 2016). Previous studies have exploited this phenomenon, especially in fiber reinforced cementitious composites (FRCC) (Honma *et al.* 2009; Nishiwaki *et al.* 2012; Cuenca and Ferrara 2017; Maddalena *et al.* 2021). Fibers can inhibit the propagation of cracks and prevent brittle failure of concrete (Li 2019). This is due to the generation of a large number of micro-cracks, which has been confirmed to be effective in self-healing of cracks (Homma *et al.* 2009). In particular, the use of polyvinyl alcohol (PVA) fibers with OH^- groups, which are polar groups, has been found to be capable of self-healing crack widths of about 0.3 mm (Nishiwaki *et al.* 2012). Furthermore, a previous study (Maddalena *et al.* 2021) has shown that the use of SCMs, which have a slower hydration reaction rate than ordinary Portland cement, can improve the self-healing performance by delayed hydration of unreacted pozzolanic material. In other words, the use of SCMs is expected to have a synergistic effect of CO_2 reduction due to reduced use of cement and extended service life of concrete structures through self-healing.

Whilst self-healing technologies have been widely investigated, their application at real-scale is limited to only few case studies for trial purposes (Gardner *et al.* 2018; Mullem *et al.* 2020). One of the reasons is the lack of a standard methods to quantitively assess the self-healing and recovery rate, as opposed to qualitative assessments (Ferrara *et al.* 2018). A quantitative evaluation of the self-healing performance is necessary to take it into account from the design stage. A number of researchers have proposed and applied their own test methods (Wang *et al.* 2019), however, a standardized method has yet to be obtained. One of the most commonly adopted test methods is visual observation of the crack width (Jakhrani *et al.* 2019). However, this method cannot identify the exact self-healing mechanism taking place within the damaged area. Therefore, it may not be possible to properly evaluate the recovery of performance such as water tightness. Other methods have also been proposed by means of water permeability (Nishiwaki *et al.* 2012) and air permeability tests (Kunieda *et al.* 2012). However, these test methods are currently only applied at laboratory level. Furthermore, laboratory tests are challenging to perform on existing materials, as they need to be tested prior and after damage. Conversely, non-destructive tests (NDT) allow to inspect the structural health of concrete elements on site by techniques such as imaging, radar and ultrasounds (Janků *et al.* 2019; Yumnam *et al.* 2021).

In this study, a new methodology based on THz wave imaging is proposed as a novel non-destructive and non-contact testing method. We evaluated the coupled self-healing performance of PVA fiber reinforced FRCC with SCM replacements. The self-healing potential of cracked concrete element (i.e., their damage recovery rate) was calculated by acquiring THz images and compared to the self-healing index obtained by microstructural observation and sorptivity tests. For the first time, THz imaging was successfully used to evaluate the self-healing performance of cracked and healed specimens.

2. Terahertz wave

Terahertz (THz) waves are electromagnetic waves in the frequency range between approximately 0.1 and 10 THz, which falls between the radio wave and the light wave frequencies, as shown in **Fig. 1**. As a result, THz waves possess characteristics of the transparency of radio wave to non-polarized materials (e.g., concrete and polymers) and the straightness and good reflectivity of infrared and visible light waves. By taking advantage of these characteristics, THz waves can non-destructively inspect the inside of insulated wires (Takahashi *et al.* 2014) and reinforced concrete structures (Tanabe and Oyama 2019) without removal of the surface covering. On the other hand, the absorption by polar molecules, such as water, is extremely high. These unique characteristics have attracted attention for applicability as NDT methods. In recent years, light sources have been developed in terms of both radio waves and light waves. In the approach as radio waves, oscillation frequencies exceeding 1 THz have been developed using resonant tunnel diodes (RTD) and other devices (Maekawa *et al.* 2016). As an approach from light waves, quantum cascade lasers and GaP-based light source have been developed, which can be operated at room temperature (Tanabe *et al.* 2003). For detectors, flexible detectors based on carbon nanotubes have been created (Suzuki *et al.* 2016). Both devices are compact

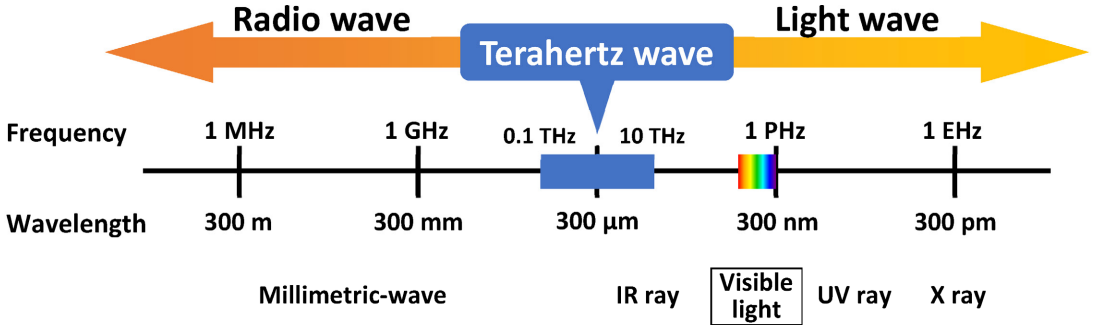

Fig. 1 Frequency range of Terahertz (THz) waves.

Table 1 Properties and physical characteristics of mix components.

Materials	Denotation	Density (g/cm^3)	Type or characteristics
Ordinary Portland cement	C	3.16	As specified in JIS R 5210:2019. Specific surface area 4170 cm^2/g.
Fine silica sand	S	2.60	Mean diameter 212 μm.
Silica fume	SF	2.20	Mean diameter 0.15 μm.
Fly ash	FA	2.23	As specified in JIS A 6201:2015 with Type II class. Specific surface area 4170 cm^2/g.
Ground granulated blast furnace slag	GGBS	2.91	As specified in JIS R 6206:2013 with 6000 cm^2/g fineness class. Specific surface area 4230 cm^2/g.
Superplasticizer	SP	1.05	Polycarboxylic acid copolymer.
PVA fiber	PVA	1.30	Diameter 40 μm, length 12 mm. Tensile strength 1560 MPa.

Table 2 Mix proportions (wt.%).

Series	B				S/B ratio	W/B ratio	SP/B ratio	PVA (vol.%)
	C	SF	FA	GGBS				
CO	100	—	—	—	40	40	0.09	2
SF	90	10	—	—				
FA	80	—	20	—				
GB	80	—	—	20				
TE	50	10	20	20				

and portable.

One THz corresponds to a quantum energy of about 4.1 meV, which is equivalent to one hundred thousandth of X-ray. Hence, it is considered safe with respect to human exposure. This energy corresponds to the intermolecular force, which is the binding energy between molecular chains. The absorption of THz waves through polar liquids can be explained based on the Drude model. As the water content increases, the transmittance decreases, and the reflectance increases. One of the authors' group has created a database of THz permeability characteristics for industrial materials, and successfully constructed non-destructive THz diagnosis system for various materials, e.g., building blocks (Oyama *et al.* 2009), insulated copper cable (Takahashi *et al.* 2014), hot-dip galvanized steel sheet (Nakamura *et al.* 2014), and moisture content of concrete material (Tanabe *et al.* 2018). Furthermore, the energy of a THz wave corresponds to molecular interactions such as hydrogen bonding, van der Waals interactions and lattice interactions. The lattice interaction is affected by a mechanical deformation of polymer. THz spectroscopy can be used for NDT of mechanical deformation in polymers (Tanabe *et al.* 2010). Non-destructive THz imaging inspection has been widely applied by by other researchers, for example, in space-shuttle ceramic style bonded state (Kharkovsky *et al.* 2007), tablet surface defect analysis (Inoue *et al.* 2003), and in the medical field, non-destructive inspection of cancer cells (Nishizawa *et al.* 2005).

In this study, THz wave transmission measurements were performed on concrete (FRCC), a non-polar material, to confirm the applicability of crack observation. The presence of water, a polar molecule, was considered as one of the experimental parameters. An attempt has been made to quantitatively evaluate the self-healing performance of cracked concrete by measuring the damaged area before and after healing. This proposed method offers a significant advantage of non-destructive and non-contact, and non-invasive measurement that can continuously apply at the same target to assess time-dependent property change. In addition, it is expected that remote measurements can be developed if a strong enough output of the THz wave is achieved. Devices with corresponding large output, e.g., Gyrotron with 37 kW, have been developed (Notake *et al.* 2009). However, they require extremely large space and low-temperature operation systems; thus, such devices are not yet readily deployable for field measurements. Nevertheless, future developments in THz technology will enable the application of such technology for in-situ building inspections.

3. Experimental procedures

3.1 Materials and mix proportions

Tables 1 and **2** show the materials used and the mix proportions. Here, FRCCs based on mortar without coarse aggregate rather than concrete were employed. There are two reasons for this; the first is to gain reliable control over the crack widths such that they remain within the limits for autogenic healing. The second is to validate the proof-of-concept THz imaging method by simplifying the cementitious system. Five series of specimens were prepared, using Portland cement and SCMs as binder at different cement replacement ratios by weight, sand, water, PVA fibers and admixtures. FRCCs were prepared with a binder content of 1187 kg/m^3, a constant water to binder ratio (W/B) of at 0.4 (475 kg/m^3), the sand to binder ratio (S/B) was also constant at 0.4 (475 kg/m^3); the superplasticizer to binder ratio (SP/B) was 0.09. All the series were mixed with PVA fibers at 2 % by volume (26 kg/m^3). The CO series with 100% ordinary Portland cement (OPC) as a binder was used as a reference. The

other four series are: SF as 10% silica fume replacement for OPC, FA as 20% fly ash replacement for OPC, GB as 20% GGBS replacement for OPC, and the TE as 50% replacement for OPC by a combination of 10% silica fume, 20% fly ash, and 20% GGBS.

3.2 Preparation of specimens

A 5-liter Omni mixer was used for mixing. After the binder and fine aggregate were dry mixed for 1 min, water and superplasticizer were added and mixed for 3 min to obtain a workable paste. A third of the PVA fibers were then added at each time, and mixed for 3 min. The paste was cast in cylindrical molds (diameter of 50 mm and height of 100 mm). The specimens were demolded at 24 hours and stored in a curing room in moist air (temperature: 20°C, relative humidity: > 90%) for 28 days from casting. The outline of the testing procedure is shown in **Fig. 2**. The specimens were tested at three conditions: [uncracked], [cracked], and [healed], the healing stage comprising 28 days placement in deionized water. During healing, each sample series was placed in a separate plastic container and the water pH was recorded at regular intervals. Note that FA and GB are expected to partially remain as unhydrated at 28 days. To confirm the effectiveness of the THz imaging method, an initial curing period of 28 days was adopted to evaluate autogenous healing subsequent to an additional 28 days of post-damage [healing]. It is acknowledged that unreacted FA and GB will be present in the cementitious matrix at first damage (28 days) and therefore any change in THz output between the damage and post damage [healed] state may result from either further pozzolanic reaction of these components or autogenous healing in the cementitious matrix. Whilst it is important to understand how different cement replacement materials influence the autogenic healing performance of the cementitious systems, the primary aim of the current study was to explore the ability of the THz imaging method to identify changes in the cementitious matrix over time. The timescales involved for damage and healing have been used in previous self-healing studies (Litina *et al.* 2021) in which distinct microstructural differences have been observed.

The self-healing performance of the specimens was evaluated by conventional sorptivity test, according to ASTM C1585, and by the new method of THz wave imaging. In addition to the basic physical properties, density and open porosity measurements, pore size distribution measurements by mercury intrusion porosimetry (MIP), and X-ray diffraction (XRD) analysis were also performed. The samples for MIP were obtained as small cubic samples, and for XRD were obtained as grounded powder from the cube samples.

3.3 Mechanical and physical properties

3.3.1 Open porosity and density

The open porosity, Φ (%) bulk density, ρ_b (g/cm^3) and matrix density ρ_m (g/cm^3) values were obtained from a vacuum saturation test performed on the damaged specimen after the compression test, according to the HAMSTAD methodology (Roels *et al.* 2004).

3.3.2 Sorptivity test

Sorptivity tests, which can be found in several previous studies (Alghamri *et al.* 2016; Zhang *et al.* 2014), were conducted to obtain the self-healing index and the recovery rate, according to the ASTM C1585. The sorptivity test was conducted three times for each specimen condition, i.e., [uncracked] as before the introduction of cracks, [cracked] as immediately after the introduction of cracks, and [healed] as after placement in deionized water for 28 days after the introduction of cracks.

At the age of 28 days, cracks were introduced by controlled cylinder splitting test using a 1000 kN universal testing machine [see **Fig. 3(a)**]. A crack mouth opening displacement (CMOD) gauge attached to the edge of the specimen was used to measure the crack width. The universal testing machine was manually controlled so that the residual CMOD was approximately 0.3 mm after unloading. During loading, the CMOD increased with the increasing load. Upon removal of load, the CMOD reduced as the specimen returns to its unloaded state, however plastic deformation in the specimen prevents this, as shown in **Fig. 3(b)**. Therefore, to achieve a CMOD of 0.3 mm at unloading, the specimens were loaded until a

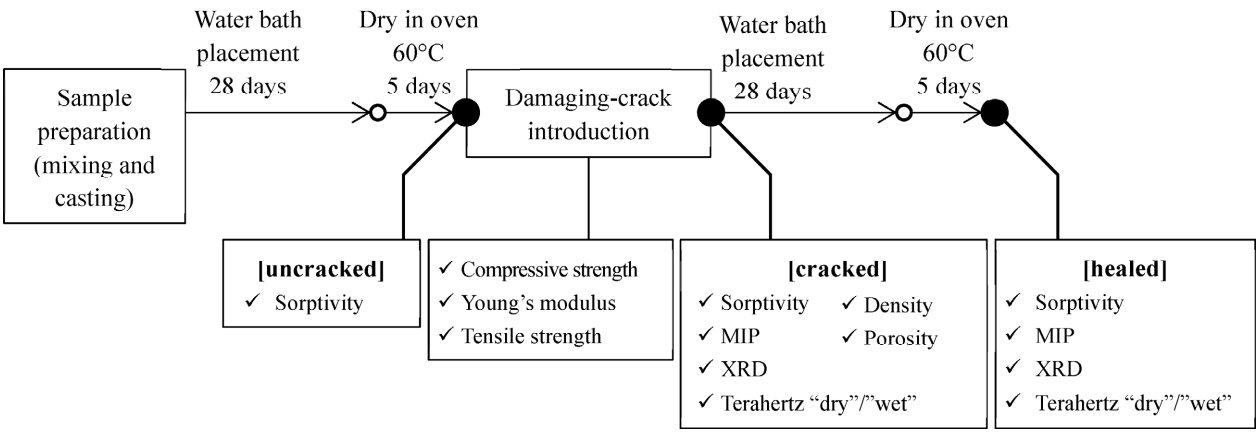

Fig. 2 Outline of the experimental plan and data collection.

CMOD of approximately 0.4 mm. The average values of the residual CMOD were 0.261 mm for series CO, 0.308 mm for SF, 0.236 mm for FA, 0.266 mm for GB and 0.249 mm for TE, with a coefficient of variation (CV) < 20%. Here, the tensile stress was calculated by Eq. (1), following the Japanese Standard JIS A 1113:2018, which is a modification of ISO 1920-4:2005.

$$\sigma_t = \frac{2 \times P}{\pi \times d \times l} \quad (1)$$

where σ_t: tensile stress [N/mm^2], P: load [N], d: diameter of the specimen [mm], and l: length of the specimen [mm].

The specimens were dried in an oven at 60°C for 5 days to equilibrate the water content of the specimens prior to the sorptivity test and prevent any microstructural damage (Gallé 2001). During the sorptivity test, the specimens were placed on spacers so that the bottom 2 mm was immersed in water. The weight of the specimens was measured with a resolution of 0.01 g at 1, 4, 9, 16, 25, 36, 49, 64, 81, and 100 min after the start of the test, respectively. The increment in weight relative to the initial weight at each measurement time was obtained and converted into the amount of water absorbed per unit area, and divided by the density of the absorbed medium (water). The absorption I (in mm) is then plotted against the square root of time, and a linear relationship is found. The gradient of the curve represents the coefficient of sorptivity (S) in mm/min$^{0.5}$. The average value from the results of 4 specimens was used as the representative value for the series.

3.3.3 Pore structure

The measurement of pore size distribution was carried out via MIP test using an AutoPore IV 9500 (Micromeritics, USA). The contact angle between the mercury and the sample was assumed to be 130°, and the surface tension of the mercury was assumed to be 0.485 N/m (Maddalena *et al.* 2021). The starting pressure was 0.0138 MPa and the ending pressure was 227.476 MPa. A 5 mm specimen for MIP analysis were sampled from the inner core of the cylinders at [cracked] and [healed] conditions. Prior to the measurement, the specimens were placed in an oven at 60 °C for 24 hours. After drying, the specimens were vacuum packed and stored in a desiccator containing silica gel until MIP measurement, to minimize carbonation and changes in the microstructure.

3.3.4 Mineralogical composition by XRD

The powder sample for XRD measurements was obtained from the 5 series of cylinders at [cracked] and [healed] conditions. The final powder was sieved to achieve an average particle size of 150 μm to prevent selective collection. The XRD samples were placed in a desiccator along with CO_2 absorbent and LiCl powder to maintain constant 11% RH until the test, following the Japanese Standard JIS C 2142:2016.

An Aeris Re (Malvern Analytical, UK) diffractometer was used to collect X-ray patterns of cracked and healed specimens. Measurements were performed with Cu light source, tube voltage of 40 kV, tube current of 15 mA,

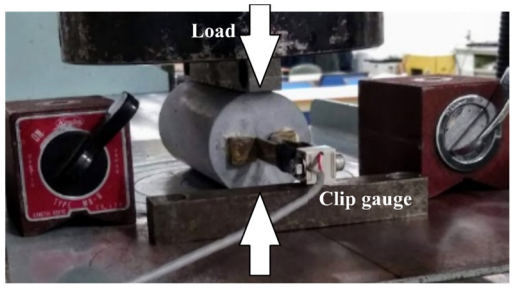

(a) Test set-up

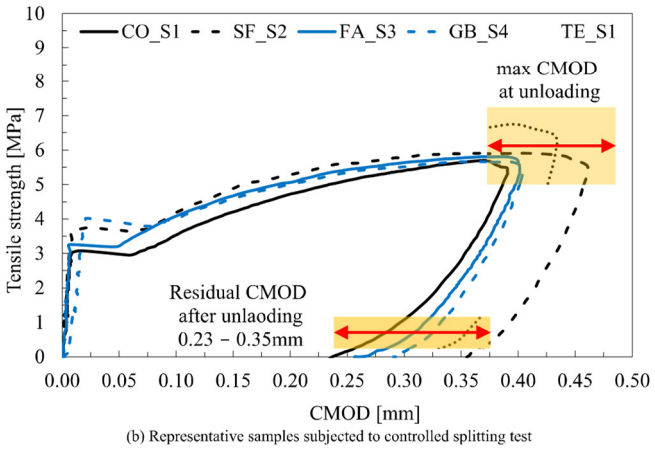

(b) Representative samples subjected to controlled splitting test

Fig. 3 Splitting tensile test to induce cracks.

scanning range of 5° to 70° (2θ), step width of approximately 0.022° (2θ), and scanning speed of 6.5°/min.

The XRD results were qualitatively analyzed with reference to the ICSD database.

3.4 Terahertz imaging for self-healing performance

Here, we propose a novel measurement method to quantitatively assess the self-healing performance by measuring the cracks before and after self-healing. That is, a visualized image representing the cracks is obtained by transmitting THz waves through the FRCC specimens. From this imaging, a quantitative evaluation method of the self-healing effect is proposed.

After the introduction of the crack with 0.3 mm residual crack, the specimens were cut into approximately 6 ± 1 mm thick discs using a small concrete saw. For each series of mixes (CO, SF, FA, GB and TE), 2 discs were imaged. A series of four measurements were made for each specimen as shown in **Fig. 4**. The first THz measurement was carried out at [cracked "dry"] conditions, which is the fully dry state after the introduction of cracks. After this first measurement, a volume of 300 μL of water was dropped on the cracks of the specimen using a micropipette to obtain the [cracked "wet"] condition. The second THz measurement was then carried out. Then, the cracked specimens were placed in deionized water for 28 days to trigger the self-healing. After the specimens were removed from the water and gently oven-dried at 60°C for 5 days, THz measurements were carried out again in the dry [healed "dry"] and wet state [healed "wet"], where 300 μL of water was dripped in the same manner as described above. The amount of water was determined by preliminary experiments as the amount that would adequately moisten the cracks.

Transmission measurements of THz waves were performed. **Figure 5** shows a diagram of the measurement system and the THz device employed. The THz waves

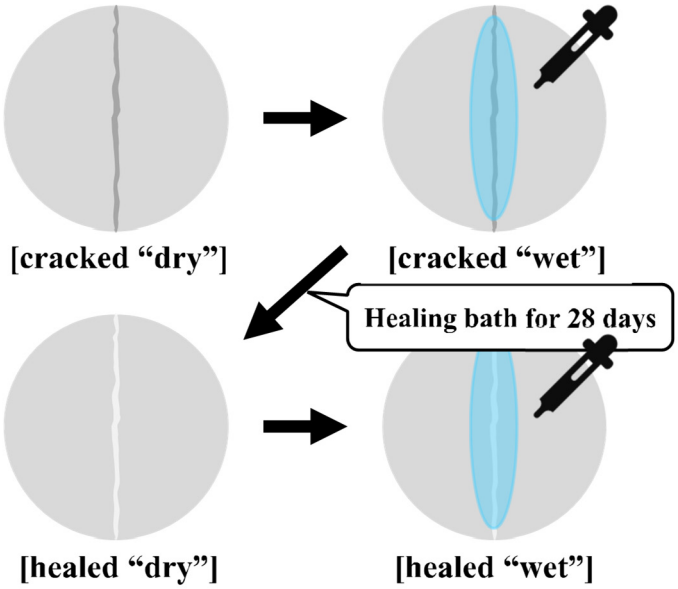

Fig. 4 Testing procedure for THz transmission measurement.

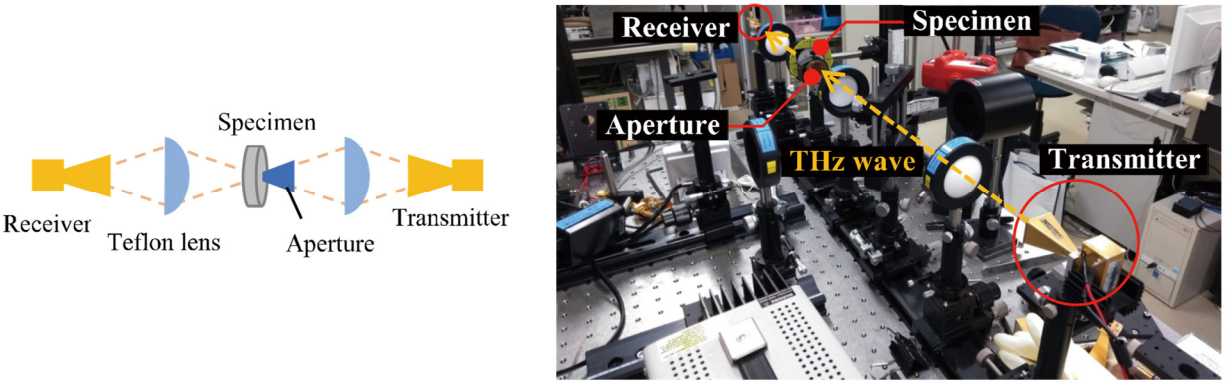

Fig. 5 (Left) Schematic diagram of the equipment used for THz wave transmission measurement, and (Right) Setup of THz wave transmission measurement.

Table 3 Average values of compressive strength (F_c), modulus of elasticity (E), tensile strength (F_t), open porosity (Φ), bulk density, (ρ_b) and matrix density (ρ_m). The numbers within brackets indicates the coefficient of variation (%).

Series	F_c [MPa]	E [GPa]	F_t [MPa]	Φ [%]	ρ_b [g/cm^3]	ρ_m [g/cm^3]
CO	60.6 (1.6)	34.4 (9.8)	4.5 (0.1)	0.28 (0.9)	1.80 (0.2)	2.49 (0.3)
SF	68.0 (0.7)	30.3 (14.4)	5.9 (8.2)	0.25 (0.2)	1.77 (0.1)	2.37 (0.0)
FA	53.2 (2.8)	28.4 (2.7)	5.9 (7.7)	0.28 (0.9)	1.76 (0.3)	2.43 (0.4)
GB	50.8 (2.9)	28.3 (3.0)	5.7 (5.6)	0.29 (0.6)	1.74 (0.2)	2.45 (0.1)
TE	63.2 (10.0)	28.9 (2.3)	6.9 (4.0)	0.23 (1.3)	1.75 (0.2)	2.29 (0.2)

emitted from the transmitter penetrate through the specimen and reach the receiver. A GUNN diode with a frequency of 90 GHz was used as the THz wave source. This frequency is slightly lower than the THz range (approximately 0.1 to 10 THz) defined in Section 2. However, it was confirmed that 90 GHz wave has similar properties to THz wave, and several previous studies referred to it as THz wave (Takahashi *et al.* 2014; Gougeon *et al.* 2019). In this work, the 90 GHz waves used here are also referred to as THz waves. To improve the resolution, an aperture with a diameter of 8 mm was placed just in front of the specimen. This device allows only the light that is focused on the surface of the sample to be extracted, while the rest of the light is cut off. The measurement area was 10 mm (length) × 20 mm (width) in the center of the specimen disk. The measurement was performed with a resolution of 0.25 mm horizontally and vertically at 3200 points in total. In the transmission measurements of THz waves, the THz wave irradiated from the transmitter penetrates the specimen, and the penetrated wave is measured as the transmission voltage at the receiver. The measured transmission voltage was converted into the transmission rate using the average value of the initial voltage measured under the same conditions without any specimens as a reference. The obtained transmission rate was color-coded according to their values, and visualized as a contour diagram.

The obtained transmission rate was further converted into a differential transmission rate to provide a clearer self-healing evaluation index. The differential transmission rate was calculated by the transmittance rate in the "dry" condition and the transmittance rate in the "wet" condition, using Eq. (2). By imaging the differential transmission rate, the state of the crack can be captured from the change in transmittance caused by the drop of water, as shown in **Fig. 6**.

$$\Delta T = T_w - T_d \,[\%] \tag{2}$$

where ΔT: differential transmission rate [%], T_w: transmission rate in "wet" condition [%], and T_d: transmission rate in "dry" condition [%].

In "dry" condition, the transmission rate becomes low at the cracks. This is due to the effect of scattering of the THz wave at the cracks. On the other hand, in "wet" condition, water diffuses around the cracks, and the THz waves are absorbed by the water, resulting in low transmission rate in and around the cracks. Based on the above, it is thought that by subtracting the transmission rate in "dry" condition from the transmission rate in "wet" condition, an image that distinguishes between cracks and the area affected by water can be obtained.

In addition, in the [healed] condition, water penetration and diffusion into the specimen in "wet" condition is suppressed due to the closure of cracks. Therefore, the influenced area by water is expected to shrink between [cracked] and [healed] conditions (Huang *et al.* 2016).

4. Results and discussion

4.1 Strength, open porosity and density

Table 3 shows the mechanical properties, and the values of density and open porosity. The average compressive strength (F_c) of CO, SF, and TE are above 60 MPa. On the other hand, the compressive strength of FA and GB is relatively low compared to that of CO. This is due to the delay in the development of compressive strength caused by the inclusion of supplementary cementitious materials.

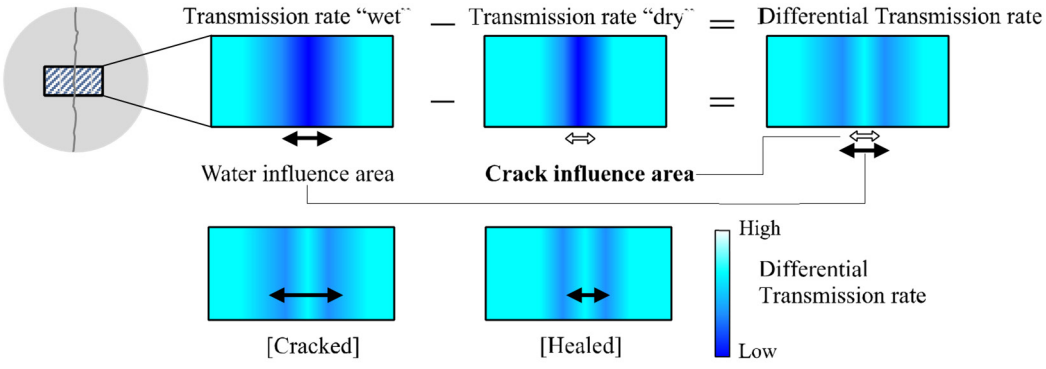

Fig. 6 Schematic diagram of differential transmission rate.

In FRCC, tensile stresses can be maintained or increased following initial cracking, due to the crack-bridging ability of the reinforcing fibers. After this initial peak, the tensile stress, gradually increased as loading continued. This increase is thought to be due to the bridging of PVA fibers, which suppresses brittle fracture. Such a response is typical of cementitious composites with polymer fibers at similar replacement levels to those used in this study (Yin *et al.* 2015). The results indicated that series TE showed the highest tensile strength (an average of 6.9 MPa), whilst samples in series CO recorded a lower strength (an average of 4.5 MPa).

The open porosity, Φ (%) bulk density, ρ_b (g/cm^3) and matrix density ρ_m (g/cm^3) values are constant throughout all series. The open porosity of CO, FA and GB is larger than SF and TE series. This is due to the presence of silica fume, which has a much smaller particle size than other replacement materials (Saraya 2014; Yildirim *et al.* 2018). Silica fume acts as a filler to fill the voids between the cement and other particles. These series are considered to have a dense microstructure with low porosity.

4.2 Self-healing performance measured by existing methods

4.2.1 Sorptivity test

The results of the sorptivity test are shown in **Fig. 7**. The sorptivity was calculated as the value per unit area divided by the bottom area of the specimen and the density of the water. The average values of four specimens were used, and the water absorption weight was converted into absorption unit (I), in mm. The [cracked] specimens in all series yielded the highest amount of water absorbed per unit area at t = 100 min (10 min$^{0.5}$) compared to the other [uncracked] and [healed] specimens. Among [cracked] conditions, FA series showed the largest I value. At [healed] conditions, the total water absorbed by samples of series SF, FA, and TE was within 5 to 10% of the [uncracked] condition, which indicates a significant densification of the microstructure and resulting in self-healing the cracks. Error bars represent the standard deviation in **Fig. 7**.

The square root of the elapsed time is proportional to

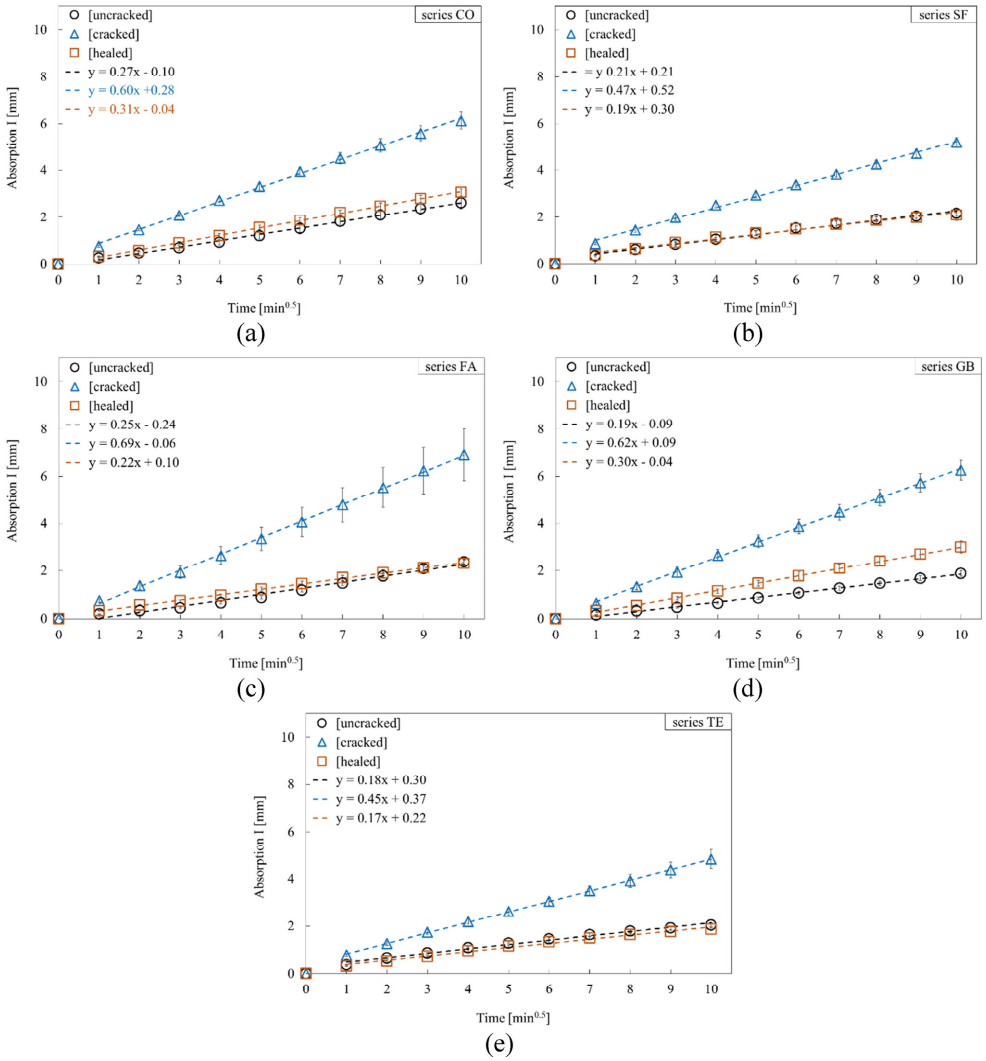

Fig. 7 Results of sorptivity test.

the amount of water absorbed, resulting in a linear relationship, and its slope is defined as the sorptivity [mm/min$^{0.5}$] in ASTM C 1585. **Figure 8** shows the values of sorptivity of each series. Sorptivity was calculated using all measured data from the beginning of the test up to 100 min. The correlation coefficient of sorptivity was greater than 0.97 for all series. From **Fig. 8**, it can be seen that sorptivity increases after cracking by 54 to 69% and decreases by 47 to 68% after healing compared to specimens at [cracked] conditions. These results suggest that the sorptivity decreased in [healed] condition due to the closure of the micro-cracks in the specimen. In addition, **Fig. 8** shows that the sorptivity of SF, FA and TE after self-healing are at the same level as those before cracking.

The recovery rate was calculated to quantify the self-healing performance. The recovery rate can be defined as the percentage that indicates the difference in sorptivity after self-healing [healed] - [cracked] compared to the difference in sorptivity after cracking [cracked] - [uncracked] as shown in Eq. (3), which is presented in a similar form to the strength recovery expression as proposed by Wang *et al.* (2019)

$$R = \frac{S_c - S_h}{S_c - S_u}\,[\%] \tag{3}$$

where R: recovery rate [%], S_u: sorptivity in [uncracked] condition, S_c: sorptivity in [cracked] condition, and S_h: sorptivity in [healed] condition.

Figure 9 shows the recovery rate of each series. From this graph, it can be seen that the recovery rate of SF, FA, and TE exceeds 100%. This may be partly attributed to the further hydration of the specimens during the 28 days of placement in water after cracking, resulting in a denser microstructure, as confirmed by MIP. Comparing the recovery rate to the specimens in series CO, it was possible to define the effect of each SCM (silica fume, fly ash and GGBS) onto the self-healing performance. Series SF, where only 10% of Portland cement was replaced by silica fume, shows a self-healing performance comparable to series FA and TE. Furthermore, series TE highlights that a higher cement replacement using a combination of SCMs offers a significant self-healing capability, as opposed to employing only a single source of SCMs.

4.2.2 Pore structure

Figure 10 shows the results of the MIP pore size distribution measurements, which were taken in the two conditions, [cracked] and [healed]. The difference observed between the two conditions for each series, and the difference between series was not significant. In all series, except for the CO series, the cumulative pore volume was larger in the [healed] condition. With respect to the pore volume distribution, the peak log differential pore volume of the series CO, FA and GB occurred at a smaller pore diameters in the [healed] condition than in the [cracked] condition. The pores refinement is due to the further reaction of SCMs during the healing stage, which is the governing autogenous healing mechanism. This resulted in existing pores being filled with hydrated products leading to a pore structure refinement (Sahmaran *et al.* 2013). The peak diameter of the log differential pore volume did not change in the [cracked] and [healed] conditions of the series made with silica fume (SF and TE). Moreover, the coarse pores in the range of 0.1 μm to 1 μm decreased and the pore volume increased in the range of diameters smaller than the peak. This can be attributed to the fact that series SF and TE (both containing silica fume) already had a finer structure than the rest of the series at [cracked] conditions, and became even denser after further exposure to water. Pores larger than 0.05 μm are considered as macropores, which are related to strength and permeability.

Table 4 shows the pore surface area (in m^2/g) of all the series at [cracked] and [healed] conditions. The values increased by 36 to 46% for all the series made with SCMs, confirming a pore refinement due to the presence of SCMs and their healing capability. Their further hydration, as opposed to samples made with only Portland cement, is one of the prominent autogenic healing mechanisms, which resulted in the precipitation of additional C-S-H and other hydrated products within the pores, thus increasing the total pore surface area after healing (Van Tittelboom *et al.* 2012; Maddalena *et al.* 2021).

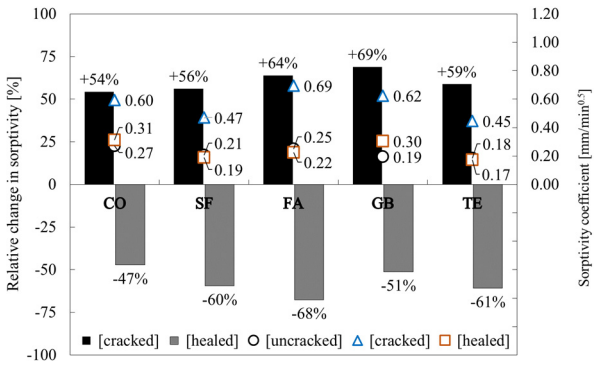

Fig. 8 Relative change in sorptivity at [cracked] and [healed] conditions, and values of sorptivity coefficient (left).

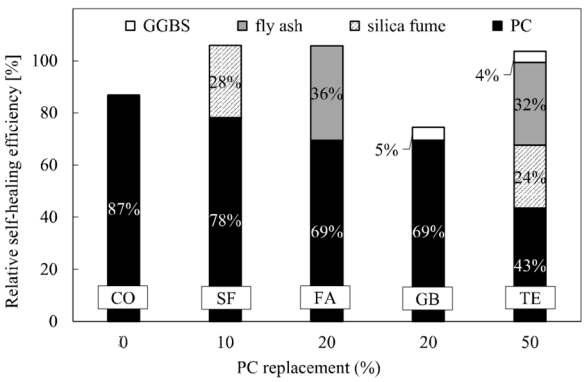

Fig. 9 Recovery rate (%) of all the series.

Table 4 Total pore surface area in m^2/g.

Series	[Cracked] m^2/g	[Healed] m^2/g	Relative change %
CO	7.8	10.0	27
SF	10.2	13.9	36
FA	8.8	12.0	35
GB	6.4	9.2	43
TE	16.0	21.6	35

4.2.3 XRD analysis and pH

XRD patterns were used to qualitatively assess the self-healing performance based on changes in the mineralogical composition between [cracked] and [healed] samples. Autogenous healing occurs by precipitation of additional C-S-H and $Ca(CO)_3$, as a result of the reaction between unreacted silica and portlandite (calcium hydroxide). **Figure 11** shows the XRD patterns of all the series, obtained at [cracked] and [healed] conditions, respectively. In series SF, FA, and TE at [healed] conditions, the peak around 26.6° (2θ), the main reflection for quartz, shows lower intensity compared to the specimens at [cracked] conditions. This is due to the pozzolanic reaction induced by the healing stage, which led to the consumption of sil-

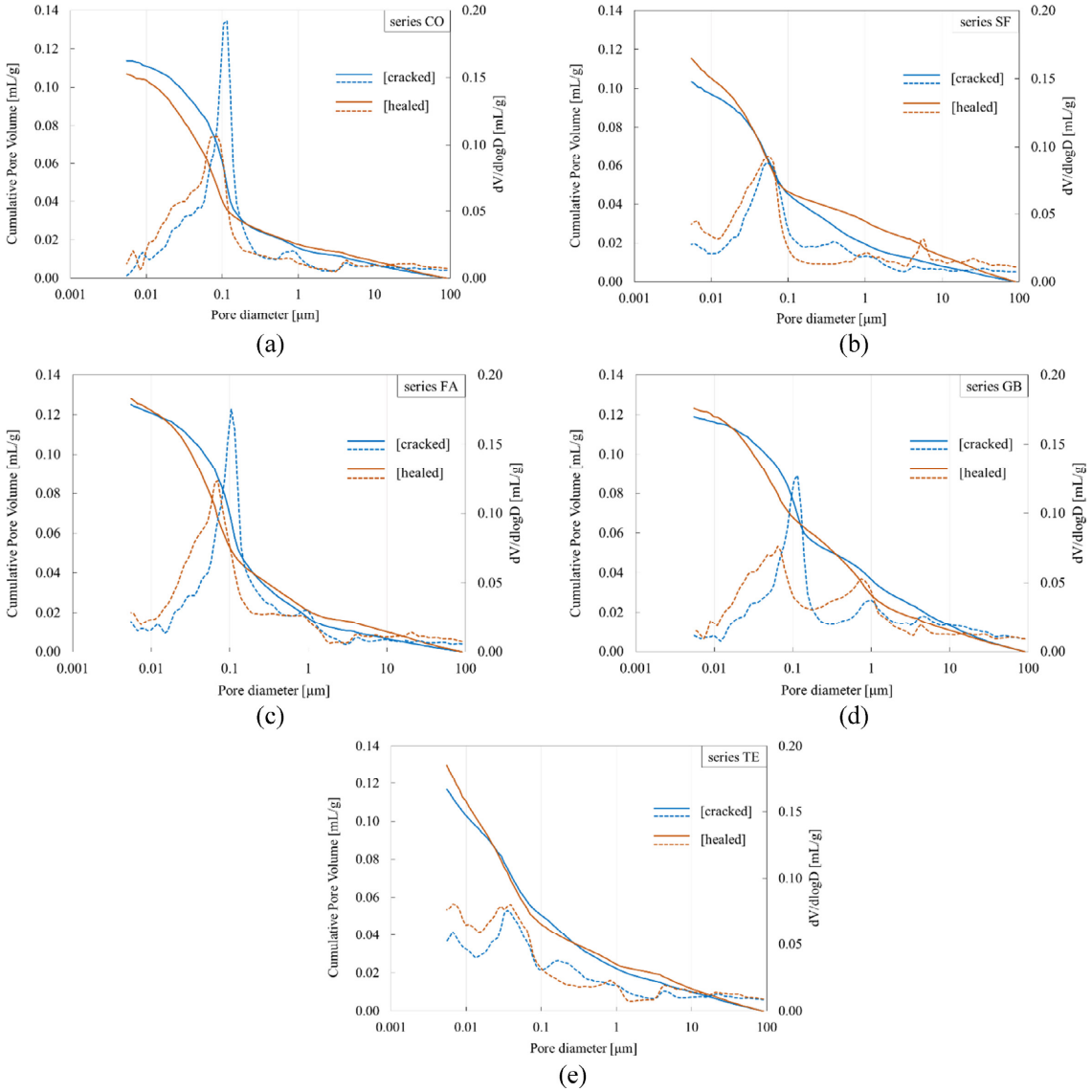

Fig. 10 Pore structure measurements at [cracked] and [healed] conditions. Straight lines represent the cumulative pore volume. Dashed lines indicate the differential volume dV/dlogD.

ica and subsequent precipitation of C-S-H. In the TE series, the portlandite reflection [observed at around 18° (2θ)] is not visible in the pattern at [healed] conditions, suggesting that the calcium hydroxide reacted with SiO_2 during the pozzolanic reaction to form additional C-S-H. In all series, the relative intensities of 29.4° and 39.4° (2θ), which are the main reflection of calcite are greater in intensity in the samples at [healed] condition than in the ones at [cracked] condition. The main peak associated to the reflection of C-S-H at approximately 29.5° (2θ) appears to be much broader in sample TE at [healed] conditions, suggesting an increased in amorphousness due to the presence of C-S-H.

During the healing stage, samples were kept in separate containers, and the pH of the water was measured at regular intervals for 28 days. The starting pH value of the water prior to immersion was 6.2. The pH data are reported in **Fig. 12**. The final values are typical of concrete pore water, in the range of 11.0 to 14.0. The pH of the healing water bath is governed by the ionic equilibrium between the water and the samples. For all the series, this equilibrium is achieved after the first 5 days. Here, the pH increases with a significantly lower rate as opposed to its rate up to day 5. A lower pH at equilibrium indicates a lower concentration of ions leached from the cementitious matrix, associated with the dissolution of available $Ca(OH)_2$ in the system (Bullard *et al.* 2010). The series TE in the graph shows a lower pH at equilibrium, suggesting that the available portlandite reacted with silica to precipitate C-S-H. This is confirmed by XRD measurements, where the peaks associated to the portlandite reflections are lower in intensity for series SF, FA and GB

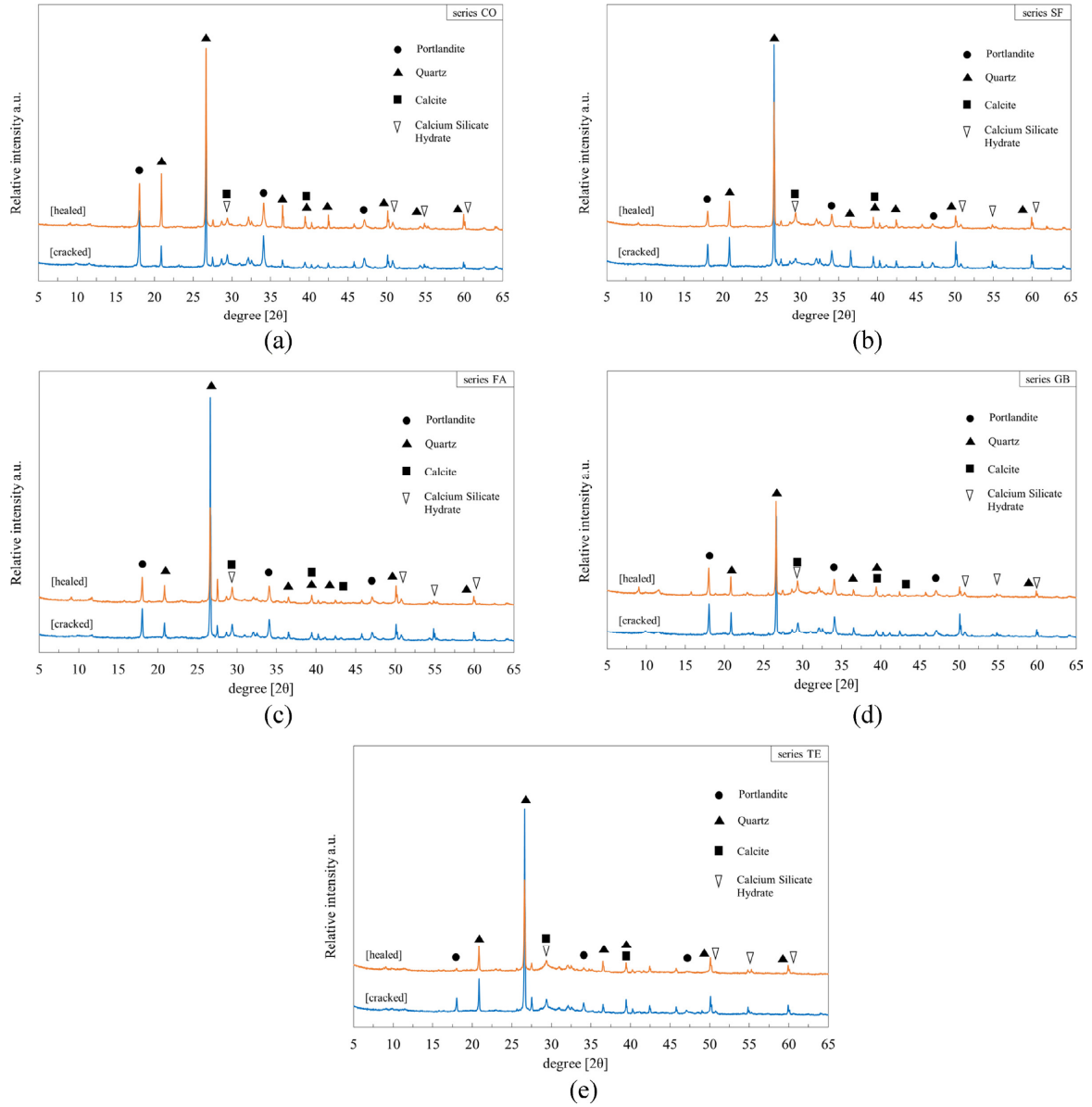

Fig. 11 XRD results for each sample series, at [cracked] and [healed] conditions. Only main mineralogical phases are indicated.

at [healed] conditions, and not visible for series TE [healed]. The pH data points were fitted to the Avrami nucleation and growth Eq. (4), commonly used to model the hydration of tricalcium and dicalcium silicate, respectively C_3S and C_2S (Ridi *et al.* 2011; Maddalena *et al.* 2019):

$$pH = c\left(1-\exp\left[-at^{n}\right]\right) \quad (4)$$

where the *pH* at time *t* is a function of *c*, a proportionality coefficient, *a*, the rate constant, and n, the coefficient associated with the nucleation and growth. The values of the coefficients, and the goodness of the fitting (R^2) are also reported in **Fig. 12**. There is a clear correlation between the Portland cement content level and the Avrami coefficient values; a decrease in Portland cement content results in a decrease in *pH*, and in turns a decrease in the values of the coefficients *a* and *c*.

4.3 Self-healing performance measured by Terahertz (THz) imaging

Examples of THz transmission images are shown in **Fig. 13**. The images presented are organized according to their cracked/healed conditions and their wet/dry state. Thus, **Figs. 13(a1)** and **(b1)** show the representative sample at [cracked "dry"] conditions. In the same manner, **Figs. 13(a2)** and **(b2)** show the [healed "dry"] conditions, **Figs. 13(a3)** and **(b3)** show the [cracked "wet"] conditions, and finally **Figs. 13(a4)** and **(b4)** show the [healed "wet"] conditions, respectively.

Comparing **Figs. 13(a1)**, **(b1)** [cracked "dry" condition] and **Figs. 13(a2)**, **(b2)** [healed "dry" condition] with **Figs. 13(a3)**, **(b3)** [cracked "wet" condition] and **Figs. 13 (a4)**, **(b4)** [healed "wet" condition], it can be seen that the darker blue area with lower transmission rate has increased. This indicates that the THz waves are absorbed by the water. In **Fig. 13(a2)**, the transmission rate is lower in the center of the measurement area of the crack than in other areas. This is due to the scattering of THz waves caused by the complex interface created by the crack.

On the other hand, the location of cracks was not clear in some specimens. For example, as shown in **Fig. 13(b1)**, the transmission rate in the dry condition varied greatly across the measurement window. This is probably due to the scattering and interference of THz waves caused by a certain variation in the thickness of the specimen and the presence of cracks. Thus, in several cases was difficult to detect cracks and evaluate the self-healing performance by using imaging transmission measurement alone.

Therefore, the THz images were processed using the differential transmission rate introduced in Eq. (2), as shown in **Figure 14**. Here, the differential transmission rate values are negative in almost all areas because the transmission rate in the dry condition is higher than that in the wet condition. In **Figs. 14(a1)** to **(a5)**, the range of low differential transmission rate is concentrated vertically in the area bounded by the gray dashed line. This is due to the water penetration and diffusion into the specimen through the cracks. Thus, this area is considered to indicate the area mostly affected by cracks. In other

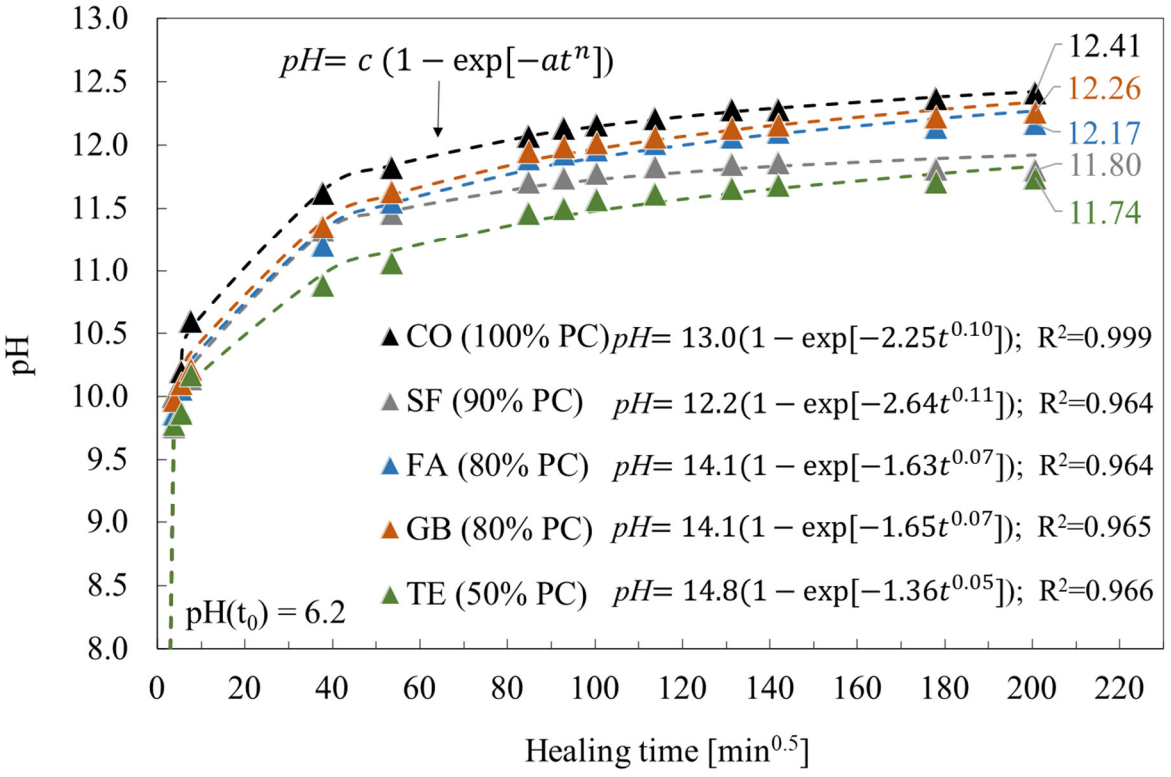

Fig. 12 pH measurement of the water during the healing bath for each sample series and curve fitting (dashed lines).

words, this area can be considered as the range of influence of moisture associated with the cracks. An index for quantitative evaluation of the moisture influence area is defined as the crack influence area. However, for simplicity of data processing, it is defined here as the crack influence area at a specific height of the images. **Figure 15** shows the results of the crack influence width calculation using **Fig. 13(a2)** as an example. The value of the differential transmission rate used for imaging is shown in the green plot (the second (right) axis), and the value of the slope obtained by differentiating this value is shown in the red plot (the first (left) axis). From the value of the slope, the inflection points of the curve showing the differential transmission rate can be determined. The area between these inflection points was defined as the crack influence area. It was confirmed that the range of the crack influence width calculated from the graphs was consistent with the crack influence area read from the images and the optical images. In addition, in the center of the crack influence area, the area where the differential transmission rate is relatively high compared to the surrounding area is distributed vertically. This area is considered as the crack area, which is also considered to correspond to the fracture process zone in fracture mechanics. This is because water is penetrating through the micro-cracks that exist in this zone. The position of the crack confirmed by the optical photograph is also shown in the figure. From these images, it can be said that the effects of the cracks and the moisture diffused around the cracks were clearly detected using the differential transmission rate for both conditions.

In **Fig. 14**, the results of the [cracked] condition are shown in the left column and the results of the [healed] condition are shown in the right column for each series. Comparing these images in two columns, it can be confirmed that the crack influence area in the [healed] condition tends to be smaller than that in the [cracked] condition. This may be attributed to the self-healing of the cracks, which closed the cracks and suppressed the water penetration and diffusion into the specimens. To evaluate this quantitatively, the change in the crack influence width before and after self-healing is defined as the self-healing recovery rate. The change in the crack influence area before and after self-healing can be calculated as the self-healing rate in the THz imaging measurement using Eq. (5).

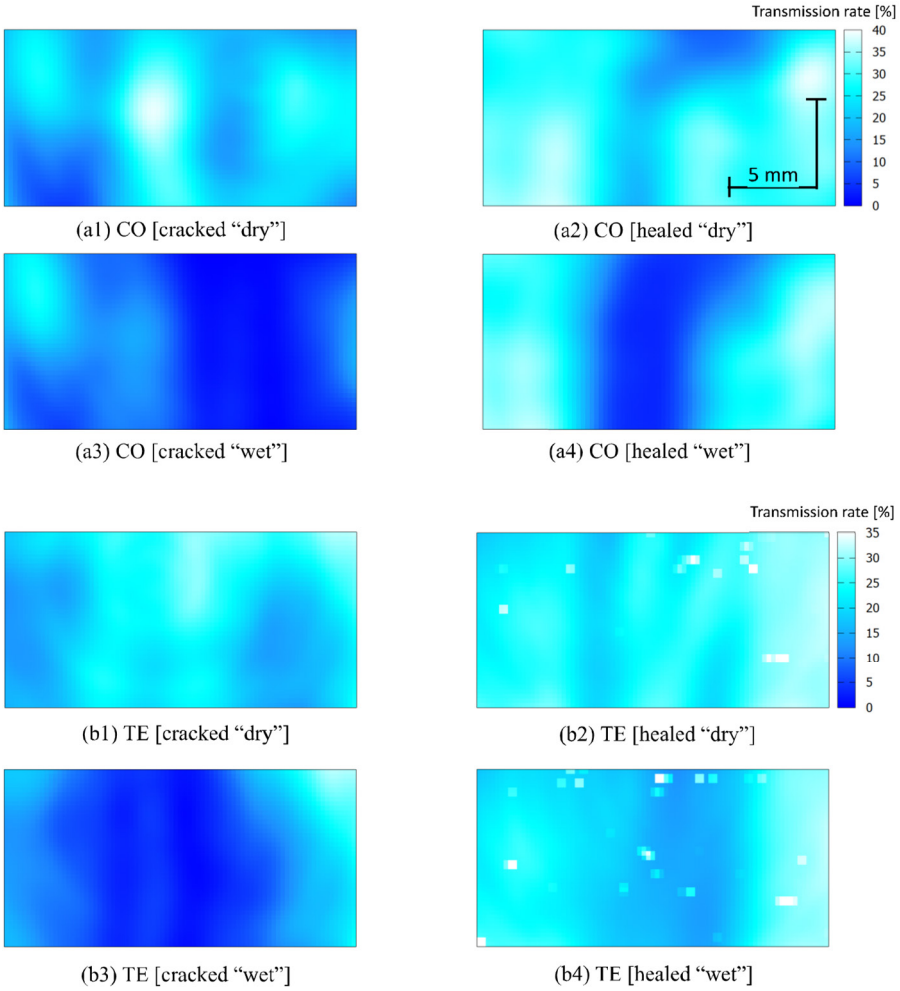

Fig. 13 Representative THz images for series CO and TE at [cracked “dry”/”wet”] and [healed “dry”/”wet”] conditions.

$$R_{\mathrm{THz}} = \left(1 - \frac{W_c}{W_h}\right) \times 100[\%] \quad (5)$$

where R_{THz}: recovery rate in THz transmission measurement [%], W_c: influence area in the [cracked] condition, W_h: influence area in the [healed] condition.

The relationship between the recovery rate calculated from the sorptivity test and the self-healing recovery rate calculated by the differential THz imaging measurement is shown in **Fig. 16**. There is a significant trend between the two recovery rates from the two types of measurements. From the definition of the recovery rate in the THz imaging measurement, the narrower the influence area, the higher the healing rate. This trend was found in the THz images of series SF and FA. In the three cases, the recovery rate exceeded 100%, resulting in the largest pore refinement (0.1 to 1 μm) and the highest amount of hydrated products after healing, as seen in the XRD patterns.

Considering these trends, the recovery rate in THz transmission measurement seems to successfully account

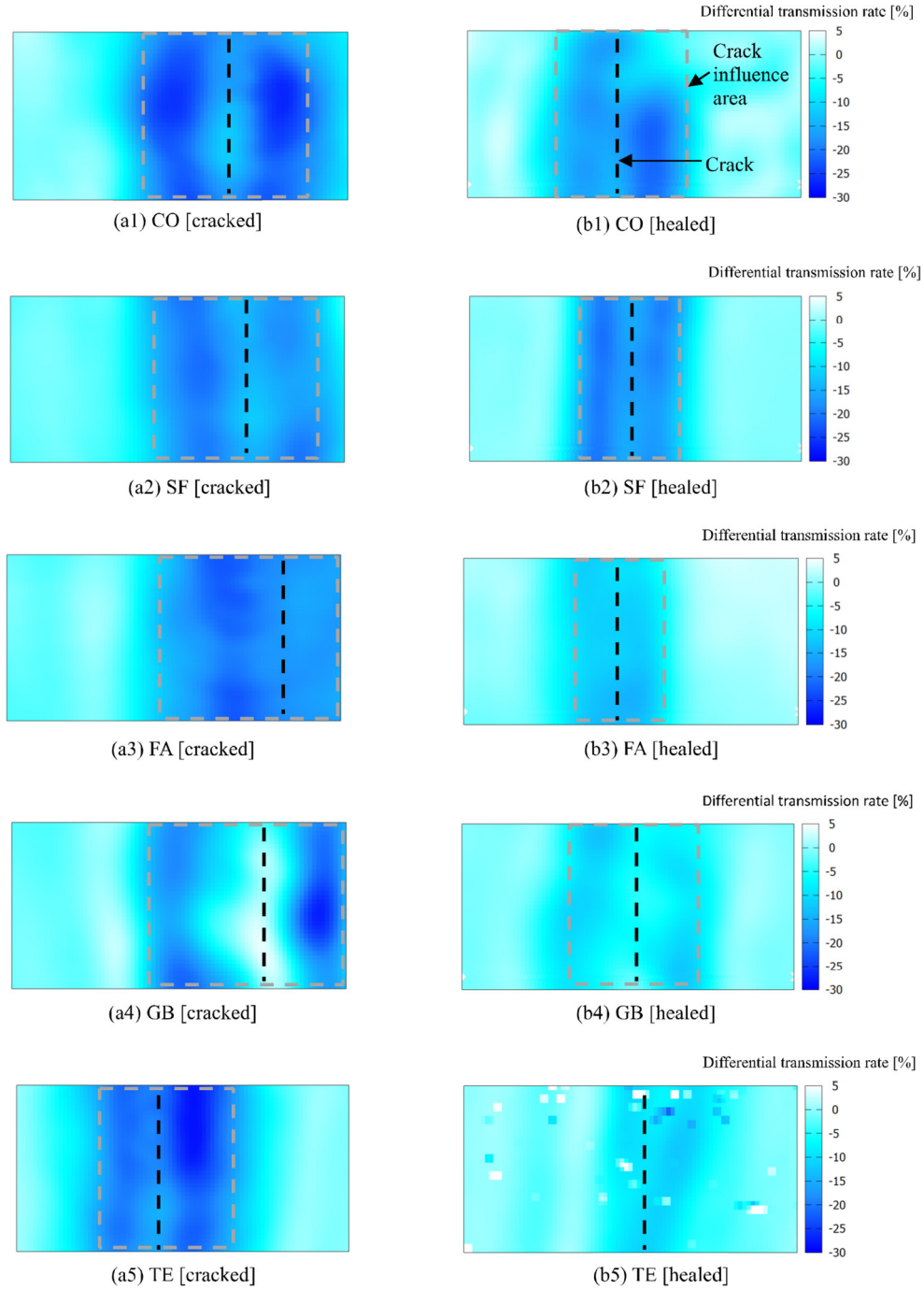

Fig. 14 Change in differential transmission rate in [cracked] and [healed] conditions.

for the self-healing potential. Thus, by taking the differential transmission rate, the self-healing effect with exposure to water could be visualized in the form of reduction of the crack influence width. Furthermore, the results of these measurements showed that the self-healing performance of FRCC can be quantitatively evaluated by calculating the self-healing rate from the reduction of the moisture influence width in the THz transmission measurement. In addition, the self-healing rate calculated from the moisture influence width showed a similar trend to the recovery rate of the sorptivity test. This suggests that THz transmission measurement may be a non-destructive alternative to the sorptivity test as an evaluation method for crack self-healing.

5. Conclusions

In this study, SCMs were used as a partial replacement of Portland cement in FRCC. The self-healing potential was investigated using conventional sorptivity test, microstructural analysis and porosimetry. A novel NDT method was also employed to study the self-healing performance of FRCC samples. For the first time, THz wave imaging was successfully used to quantify the self-healing performance on cementitious samples. The following conclusions can be drawn:

(1) Sorptivity tests were conducted on FRCC using PVA fiber in three conditions: before the introduction of cracks [uncracked], after the introduction of cracks [cracked], and after 28 days of placement in water for self-healing [healed]. In addition, the self-healing effect was quantitatively evaluated.

(2) Pore size distribution measurement showed that SCMs contributed to the largest pore refinement at [healed] conditions compared to [cracked] samples.

(3) XRD results showed that the pozzolanic reaction

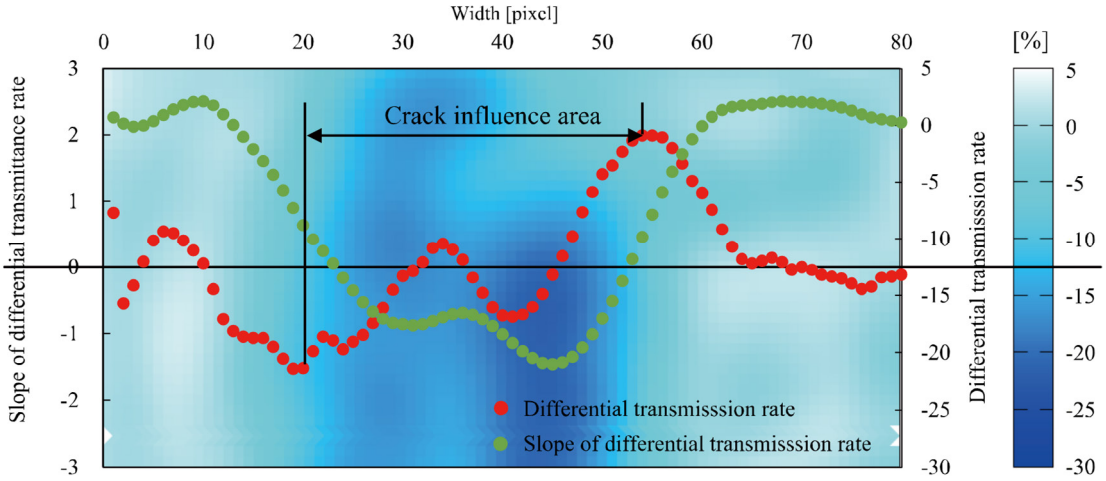

Fig. 15 Example of quantitative evaluation of the crack influence area, represented on the sample CO [healed “dry”].

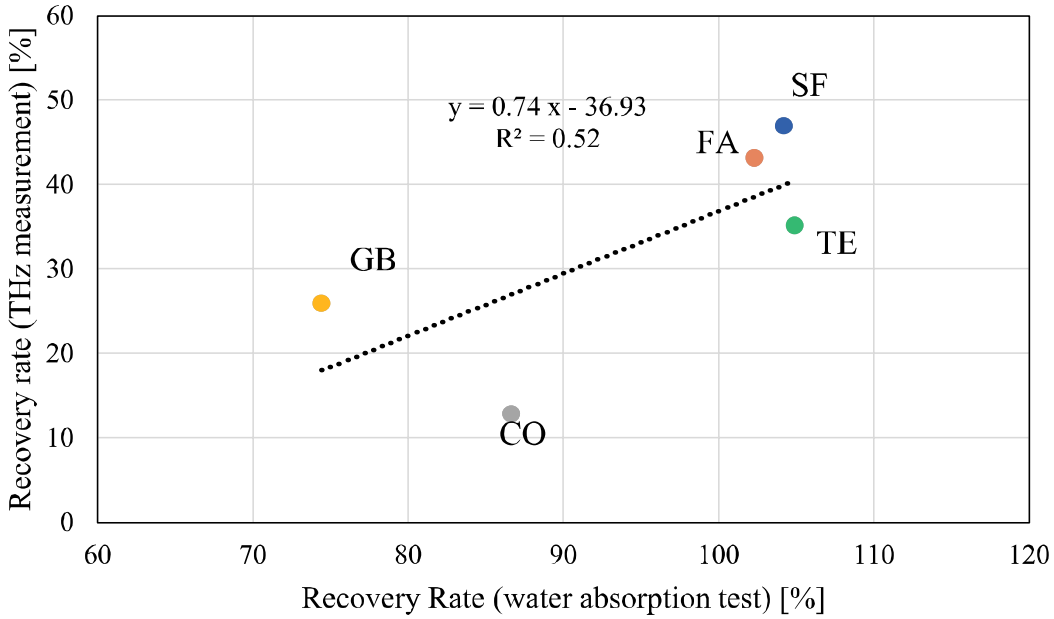

Fig. 16 Recovery rate (sorptivity test) vs recovery rate (THz measurement).

progressed in SF, FA and TE after cracking and placement in water. The relative intensity of calcite increased after self-healing in all series, suggesting the precipitation of calcium carbonate after self-healing.

(4) THz imaging measurements showed that it is possible to describe the state of cracks from the differential transmittance obtained using water as a sensitizer.

(5) The crack influence width can be calculated from the differential transmittance obtained by THz imaging measurement. Furthermore, the self-healing rate can be calculated from the change in the crack influence width, and the correlation with the self-healing rate obtained from the sorptivity test was confirmed. In other words, it was suggested that the self-healing property of FRCC could be quantitatively evaluated by THz imaging measurement.

The preliminary results presented in this study demonstrate the potential of THz spectroscopy as a non-destructive technique to be employed in in-situ applications. However, current limitations in THz wave outputs devices suggest that further work is needed to optimize the technology before being deployed in the field for in-situ inspections.

Acknowledgements

This work was supported by the Japan Society for Promotion of Science (JSPS) Postdoctoral Fellowship (grant number PE19722), and associated JSPS Grants-in-Aid for Scientific Research-KAKENHI. The support of the UKRI-EPSRC funded Resilient Materials 4 Life, RM4L (grant number EP/P02081X/1) is also acknowledged.

References

Alghamri, R., Kanellopoulos, A. and Al-Tabbaa, A., (2016). "Impregnation and encapsulation of lightweight aggregates for self-healing concrete." *Construction and Building Materials*, 124, 910-921.

Andrew, R. M., (2019). "Global CO_2 emissions from cement production, 1928-2018." *Earth System Science Data*, 11(4), 1675-1710.

Bullard, J. W., Enjolras, E., George, W. L., Satterfield, S. G. and Terrill, J. E., (2010). "A parallel reaction-transport model applied to cement hydration and microstructure development." *Modelling and Simulation in Materials Science and Engineering*, 18(2), 025007.

Cuenca, E. and Ferrara, L., (2017). "Self-healing capacity of fiber reinforced cementitious composites. State of the art and perspectives." *KSCE Journal of Civil Engineering*, 21(7), 2777-2789.

Davies, R., Teall, O., Pilegis, M., Kanellopoulos, A., Sharma, T., Jefferson, A., Gardner, D., Al-Tabbaa, A., Paine, K. and Lark, R., (2018). "Large scale application of self-healing concrete: design, construction, and testing." *Frontiers in Materials*, 5, 00051.

De Belie, N., Gruyaert, E., Al-Tabbaa, A., Antonaci, P., Baera, C., Bajare, D., Darquennes, A., Davies, R., Ferrara, L., Jefferson, T., Litina, C., Miljevic, B., Otlewska, A., Ranogajec, J., Roig-Flores, M., Paine, K., Lukowski, P., Serna, P., Tulliani, J. M., Vucetic, S., Wang, J. and Jonkers, H. M., (2018). "A review of self-healing concrete for damage management of structures." *Advanced Materials Interfaces*, 5(17), 1-28.

Edvardsen, C., (1999). "Water permeability and autogenous healing of cracks in concrete." *ACI Materials Journal*, 96, 448-454.

Ellis, L. D., Badel, A. F., Chiang, M. L., Park, R. J.-Y. and Chiang, Y.-M., (2019). "Toward electrochemical synthesis of cement - An electrolyzer-based process for decarbonating $CaCO_3$ while producing useful gas streams." *Proceedings of the National Academy of Sciences*, 117(23), 12584-12591.

Ferrara, L., Van Mullem, T., Alonso, M. C., Antonaci, P., Borg, R. P., Cuenca, E., Jefferson, A., Ng, P. L., Peled, A., Roig-Flores, M., Sanchez, M., Schroefl, C., Serna, P., Snoeck, D., Tulliani, J. M. and De Belie, N., (2018). "Experimental characterization of the self-healing capacity of cement based materials and its effects on the material performance: A state of the art report by COST Action SARCOS WG2." *Construction and Building Materials*, 167, 115-142.

Gallé, C., (2001). "Effect of drying on cement-based materials pore structure as identified by mercury intrusion porosimetry." *Cement and Concrete Research*, 31(10), 1467-1477.

Gardner, D., Lark, R., Jefferson, T. and Davies, R., (2018). "A survey on problems encountered in current concrete construction and the potential benefits of self-healing cementitious materials." *Case Studies in Construction Materials*, 8, 238-247.

Gougeon, G., Corre, Y. and Aslam, M. Z., (2019). "Sub-THz channel characterization from ray-based deterministic simulations." *ITU Journal*, 2(1), 17-25.

Honma, D., Mihashi, H., Mizukami, T. and Nishiwaki, T., (2009). "Experimental study on the self-healing capability of fiber reinforced cementitious composites." In: T. Tanabe, K. Sakata, H. Mihashi, R. Sato, K. Maekawa and H. Nakamura, Eds. *Proc. 8th International. Conference on Creep, Shrinkage and Durability Mechanics of Concrete and Concrete Structures*, Ise-Shima, Japan 30 September - 2 October. London and New York: CRC Press, 1, 769-774.

Huang, H., Ye, G., Qian, C. and Schlangen, E., (2016). "Self-healing in cementitious materials: Materials, methods and service conditions." *Materials & Design*, 92, 499-511.

Inoue, H., Kawase, K., Ogawa, Y. and Watanabe, Y., (2003). "Non-destructive terahertz imaging of illicit drugs using spectral fingerprints." *Optics Express*, 11(20), 2549-2554.

Jakhrani, S. H., Qudoos, A., Kim, H. G., Jeon, I. K. and Ryou, J. S., (2019). "Review on the self-healing

concrete-approach and evaluation techniques." *Journal of Ceramic Processing Research*, 20(S1), 1-18.

Janků, M., Cikrle, P., Grošek, J., Anton, O. and Stryk, J., (2019). "Comparison of infrared thermography, ground-penetrating radar and ultrasonic pulse echo for detecting delaminations in concrete bridges." *Construction and Building Materials*, 225, 1098-1111.

JSCE, (2002). "*Report of the subcommittee on assessment for environmental impact of concrete* (Concrete Engineeering Series 44)." Tokyo: Japan Society of Civil Engineers.

Kharkovsky, S., Zoughi, R. and Hepburn, F., (2007). "High resolution millimeter wave detection of vertical cracks in the space shuttle external tank spray-on-foam insulation (SOFI)." *AIP Conference Proceedings*, 894, 1065-1070.

Kunieda, M., Choonghyun, K., Ueda, N. and Nakamura, H., (2012). "Recovery of protective performance of cracked ultra high performance-strain hardening cementitious composites (UHP-SHCC) due to autogenous healing." *Journal of Advanced Concrete Technology*, 10(9), 313-322.

Li, V. C., (2019). "*Engineered cementitious composites (ECC)*." Berlin and Heidelberg: Springer.

Litina, C., Bumanis, G., Anglani, G., Dudek, M., Maddalena, R., Amenta, M., Papaioannou, S., Pérez, G., García Calvo, J. L., Asensio, E., Beltrán Cobos, R., Tavares Pinto, F., Augonis, A., Davies, R., Guerrero, A., Sánchez Moreno, M., Stryszewska, T., Karatasios, I., Tulliani, J.-M., Antonaci, P., Bajare, D. and Al-Tabbaa, A., (2021). "Evaluation of methodologies for assessing self-healing performance of concrete with mineral expansive agents: An interlaboratory study." *Materials*, 14(8), 2024.

Maddalena, R., Hall, C. and Hamilton, A., (2019). "Effect of silica particle size on the formation of calcium silicate hydrate [C-S-H] using thermal analysis." *Thermochimica Acta*, 672, 142-149.

Maddalena, R., Taha, H. and Gardner, D., (2021). "Self-healing potential of supplementary cementitious materials in cement mortars: Sorptivity and pore structure." *Developments in the Built Environment*, 6, 100044.

Maekawa, T., Kanaya, H., Suzuki, S. and Asada, M., (2016). "Oscillation up to 1.92 THz in resonant tunneling diode by reduced conduction loss." *Applied Physics Express*, 9(2), 024101.

Mihashi, H. and Nishiwaki, T., (2012). "Development of engineered self-healing and self-repairing concrete-state-of-the-art report." *Journal of Advanced Concrete Technology*, 10(5), 170-184.

Mullem, T. Van, Gruyaert, E., Caspeele, R. and De Belie, N., (2020). "First large scale application with self-healing concrete in Belgium: Analysis of the laboratory control tests." *Materials*, 13(4), 0997.

Müller, H. S., Haist, M. and Vogel, M., (2014). "Assessment of the sustainability potential of concrete and concrete structures considering their environmental impact, performance and lifetime." *Construction and Building Materials*, 67, Part C, 321-337.

Nakamura, Y., Kariya, H., Sato, A., Tanabe, T., Nishihara, K., Taniyama, A., Nakajima, K., Maeda, K. and Oyama, Y., (2014). "Nondestructive corrosion diagnosis of painted hot-dip galvanizing steel sheets by using THz spectral imaging." *Corrosion Engineering (Zairyo to Kankyo)*, 63(9), 411-416. (in Japanese)

Nishiwaki, T., Koda, M., Yamada, M., Mihashi, H. and Kikuta, T., (2012). "Experimental study on self-healing capability of FRCC using different types of synthetic fibers." *Journal of Advanced Concrete Technology*, 10(6), 195-206.

Nishizawa, J. I., Sasaki, T., Suto, K., Yamada, T., Tanabe, T., Tanno, T., Sawai, T. and Miura, Y., (2005). "THz imaging of nucleobases and cancerous tissue using a GaP THz-wave generator." *Optics Communications*, 244(1-6), 469-474.

Notake, T., Saito, T., Tatematsu, Y., Fujii, A., Ogasawara, S., Agusu, L., Ogawa, I., Idehara, T. and Manuilov, V. N., (2009). "Development of a novel high power sub-THz second harmonic gyrotron." *Physical Review Letters*, 103(22), 225002.

Oyama, Y., Zhen, L., Tanabe, T. and Kagaya, M., (2009). "Sub-terahertz imaging of defects in building blocks." *NDT & E International*, 42(1), 28-33.

Ridi, F., Fratini, E. and Baglioni, P., (2011). "Cement: A two thousand year old nano-colloid." *Journal of Colloid and Interface Science*, 357(2), 255-64.

Roels, S., Carmeliet, J., Hens, H., Adan, O., Brocken, H., Cerny, R., Pavlik, Z., Hall, C., Kumaran, K., Pel, L. and Plagge, R., (2004). "Interlaboratory comparison of hygric properties of porous building materials." *Journal of Building Physics*, 27(4), 307-325.

Sahmaran, M., Yildirim, G. and Erdem, T. K., (2013). "Self-healing capability of cementitious composites incorporating different supplementary cementitious materials." *Cement and Concrete Composites*, 35(1), 89-101.

Saraya, M. E.-S. I., (2014). "Study physico-chemical properties of blended cements containing fixed amount of silica fume, blast furnace slag, basalt and limestone, a comparative study." *Construction and Building Materials*, 72, 104-112.

Schneider, M., Romer, M., Tschudin, M. and Bolio, H., (2011). "Sustainable cement production - Present and future." *Cement and Concrete Research*, 41(7), 642-650.

Suzuki, D., Oda, S. and Kawano, Y., (2016). "A flexible and wearable terahertz scanner." *Nature Photonics*, 10(12), 809-813.

Takahashi, S., Hamano, T., Nakajima, K., Tanabe, T. and Oyama, Y., (2014). "Observation of damage in insulated copper cables by THz imaging." *NDT & E International*, 61, 75-79.

Tanabe, T., Kanai, T., Kuroo, K., Nishiwaki, T. and Oyama, Y., (2018). "Non-contact terahertz inspection

of water content in concrete of infrastructure buildings." *World Journal of Engineering and Technology*, 6(02), 275-281.

Tanabe, T. and Oyama, Y., (2019). "THz non-destructive visualization of disconnection and corrosion status covered with opaque insulator." *IEEJ Transactions on Electronics, Information and Systems*, 139(2), 149-153.

Tanabe, T., Suto, K., Nishizawa, J., Saito, K. and Kimura, T., (2003). "Tunable terahertz wave generation in the 3- to 7-THz region from GaP." *Applied Physics Letters*, 83(2), 237.

Tanabe, T., Watanabe, K., Oyama, Y. and Seo, K., (2010). "Polarization sensitive THz absorption spectroscopy for the evaluation of uniaxially deformed ultra-high molecular weight polyethylene." *NDT & E International*, 43(4), 329-333.

Van Tittelboom, K., Gruyaert, E., Rahier, H. and De Belie, N., (2012). "Influence of mix composition on the extent of autogenous crack healing by continued hydration or calcium carbonate formation." *Construction and Building Materials*, 37, 349-359.

Wang, X. F., Yang, Z. H., Fang, C., Han, N. X., Zhu, G. M., Tang, J. N. and Xing, F., (2019). "Evaluation of the mechanical performance recovery of self-healing cementitious materials - Its methods and future development: A review." *Construction and Building Materials*, 212, 400-421.

Yang, K. H., Jung, Y. B., Cho, M. S. and Tae, S. H., (2015). "Effect of supplementary cementitious materials on reduction of CO_2 emissions from concrete." *Journal of Cleaner Production*, 103, 774-783.

Yildirim, G., Khiavi, A. H., Yesilmen, S. and Sahmaran, M., (2018). "Self-healing performance of aged cementitious composites." *Cement and Concrete Composites*, 87, 172-186.

Yin, S., Tuladhar, R., Shi, F., Combe, M., Collister, T. and Sivakugan, N., (2015). "Use of macro plastic fibres in concrete: A review." *Construction and Building Materials*, 93, 180-188.

Yumnam, M., Gupta, H., Ghosh, D. and Jaganathan, J., (2021). "Inspection of concrete structures externally reinforced with FRP composites using active infrared thermography: A review." *Construction and Building Materials*, 310, 125265.

Zhang, Z., Qian, S. and Ma, H., (2014). "Investigating mechanical properties and self-healing behavior of micro-cracked ECC with different volume of fly ash." *Construction and Building Materials*, 52, 17-23.